exchange-integral effects tend to be dominated by terms of lower L. In addition, there is a phase factor πL associated with the asymptotic behavior of term with given L. Seeing the enhancement of the Friedel oscillations, when $L=3$ interband mixing is added to the electrostatic exchange polarization, one might anticipate a cancellation for the case of a transition-metal local moment with its $L=2$ mixing. While there may be such a tendency for such a case, it should be noted that *both even- and odd-L* partial waves are involved in the exchange-integral term.[10,11] This affects the frequently made assumptions that the asymptotic form for the Friedel oscillations holds quite accurately on into the main peak, and that the amplitude of the oscillations faithfully reflects the net induced spin. It is clear from our results that we have a case where neither assumption is valid. They are probably a far better approximation when dealing with transition-metal moments, but they will never be rigorously correct when both interband mixing and electrostatic exchange scattering are present.

ACKNOWLEDGMENTS

We wish to thank E. Wolfson for her assistance with the computer calculations and to acknowledge communication with A. M. Clogston, M. Peter, and J. R. Schrieffer.

PHYSICAL REVIEW VOLUME 186, NUMBER 3 15 OCTOBER 1969

Magnetoacoustic Effects in Very Pure Cd*†

J. D. GAVENDA AND F. H. S. CHANG‡
Department of Physics, University of Texas, Austin, Texas 78712
(Received 15 May 1969)

Ultrasonic attenuation as a function of magnetic field intensity has been measured in very pure Cd at liquid-helium temperatures. The results are related to the dimensions of the Fermi surface using the usual phenomenological model for the magnetoacoustic effect. New resonances are observed, and an explanation in terms of cylindrical sections of the Fermi surface is offered. Finally, evidence for acoustic cyclotron resonance is presented, along with comments on the observation and interpretation of such phenomena.

I. INTRODUCTION AND THEORY

ALTHOUGH there have been a number of earlier studies of the magnetoacoustic effect in Cd,[1–3] there has not been good agreement between the dimensions quoted by the different workers for certain parts of the Fermi surface. Also, some parts observed by other experimental techniques[4] have not been found using the magnetoacoustic effect. We have used very pure single crystals of Cd in an attempt to clarify the situation.

In carrying out these experiments, we have found some rather interesting "line shapes" which appear to be the result of very long electron mean free paths and relaxation times. In particular, it appears that a cylindrical section of the Fermi surface is responsible for some very pronounced resonance peaks in the attenuation over a restricted angular range.

Before presenting the experimental data, we will summarize the principal results of the free-electron theory for the magnetoacoustic effect, using the notation of Cohen, Harrison, and Harrison.[5]

For a magnetic field $\mathbf{B}$ perpendicular to the sound-propagation vector $\mathbf{q}$, the attenuation can be expressed as

$$\alpha_i=(mv_F/Mv_s)S_{ii}/l, \quad (1)$$

where $i=1$ for compressional waves, $i=2$ for shear waves polarized perpendicular to $\mathbf{B}$, $i=3$ for shear waves polarized parallel to $\mathbf{B}$, m is the electron mass, M the ion mass, v_F the electron Fermi velocity, v_s the sound velocity, and l the electron mean free path. The tensor elements S_{ii} are defined by

$$S_{11}=\sigma_0\,\mathrm{Re}[\sigma_{22}/(\sigma_{11}\sigma_{22}+\sigma_{12}^2)]-q^2l^2/3(1+\omega^2\tau^2)-1, \quad (2)$$

$$S_{22}=\sigma_0\,\mathrm{Re}[\sigma_{11}/(\sigma_{11}\sigma_{22}+\sigma_{12}^2)]-1, \quad (3)$$

$$S_{33}=\sigma_0\,\mathrm{Re}(1/\sigma_{33})-1, \quad (4)$$

where σ_0 is the dc conductivity, $\omega=2\pi\nu$ is the sound frequency, and τ the relaxation time. The conductivity-tensor elements are defined in Appendix A. We have assumed here that $\omega c^2/4\pi\sigma_0 v_s^2\ll 1$, where c is the velocity of light. A plot of S_{11} for $\omega\tau\ll 1$ is shown in Fig. 1(a).

* Work supported by a grant from the National Science Foundation.
† Based in part on a Ph.D. dissertation by F. H. S. Chang, University of Texas, 1966 (unpublished).
‡ Present address: Florida Institute of Technology, Melbourne, Fla. 32901.
[1] B. C. Deaton, Ph.D. dissertation, University of Texas, 1962 (unpublished).
[2] M. R. Daniel and L. Mackinnon, Phil. Mag. **8**, 537 (1963).
[3] D. F. Gibbons and L. M. Falicov, Phil. Mag. **8**, 177 (1963).
[4] J. K. Galt, F. R. Merritt, and J. R. Klauder, Phys. Rev. **139**, A823 (1965).
[5] M. H. Cohen, M. J. Harrison, and W. A. Harrison, Phys. Rev. **117**, 937 (1960).

The elements of the conductivity tensor are expressible as sums of cylindrical Bessel functions $J_n(X)$, where $X=qv_F/\omega_c=2\pi R_F/\lambda$, $\omega_c=eB/mc$, R_F is the radius of the orbit for an electron moving perpendicular to **B** with speed v_F, and λ is the sound wavelength. The period of the oscillations shown in Fig. 1 corresponds to a change in X by an amount π, or a change in orbit diameter by 1 wavelength of sound. For a general Fermi surface, one expects oscillations with periods determined by extremal diameters of the Fermi surface in the direction $\mathbf{q}\times\mathbf{B}$.[6] This is the assumption used in interpreting the experimental data in the following sections.

The spherical Fermi surface yields a Bessel function like behavior of α versus B. However, other line shapes are possible for nonspherical Fermi surfaces. In particular, open-orbit electrons moving along **q** in real space yield sharp resonances.[7] This is because all of the open orbits have precisely the same period (determined by the reciprocal-lattice dimension) and therefore come into resonance with the sound wave at the same magnetic field value.

One would expect to observe sharp resonances in α for a Fermi surface with a constant extremal diameter (or caliper) over a finite range of k_B, the component of **k** parallel to **B**. A simple model for calculating such

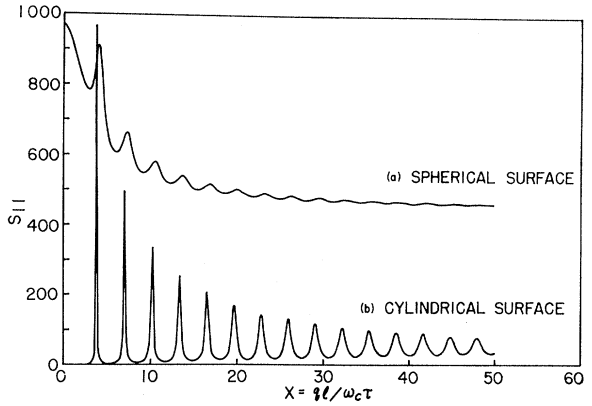

FIG. 1. Calculated attenuation for spherical and cylindrical Fermi surfaces for $ql=100$, $\omega\tau=0$, or $v_s/v_F=0$. The curve for the spherical surface has been shifted upward by 300.

effects is a cylindrical Fermi surface with axis along **B**. The calculations, which are summarized in Appendix B, reduce to a two-dimensional problem. The results, which turn out to be identical for compressional waves and for shear waves polarized perpendicular to **B**, are shown in Fig. 1(b) for the limit $v_s/v_F\rightarrow 0$ or for $\omega\tau\rightarrow 0$.

The resonances can be explained by looking at the form of S_{11} for $ql\gg 1$, $\omega_c^2\tau^2\gg 1$, $\omega\tau\gg 1$,

$$S_{11}=\tfrac{1}{2}q^2l^2\frac{\sum[J_0(X)J_n'(X)+J_1(X)J_n(X)]^2/n^2}{(q^2l^2/2X^2)J_1^2(X)+\sum[J_n'(X)/n]^2-\sum[J_0(X)J_n'(X)+J_1(X)J_n(X)]^2/n^2}, \tag{5}$$

where all sums are from $n=1$ to ∞.

For $q^2l^2/2X^2\gg 1$, S_{11} will be small except near the roots of $J_1(X)$. Near the roots X_1 resonant behavior will be found with maxima

$$S_{11}^{\rm res}=\tfrac{1}{2}q^2l^2J_0^2(X_1)/[1-J_0^2(X_1)]. \tag{6}$$

Within the approximations stated above, the heights of the resonances will be proportional to q^2l^2 and the widths inversely proportional to ql. (See Appendix B for further discussion of this result.)

The effect of finite $\omega\tau$ is to split the resonance peaks as a result of Doppler shift. In Fig. 2, this effect has been exaggerated by the use of a rather small value for the ratio of v_F/v_s. In order to observe the splitting experimentally, one needs a very pure specimen so that $\omega\tau\gtrsim 1$, and **B** must be precisely perpendicular to **q**. In Sec. III, we report the observation of resonance peaks which we attribute to cylindrical sections of the Fermi surface of Cd.

II. EXPERIMENTAL METHODS

A standard pulsed ultrasonic technique[8] was used in the measurements. The transducers were X-cut for compressional waves, AC-cut for shear waves, and had fundamental resonances near 10 MHz. The transducers were bonded to the specimens with Nonaq stopcock grease.

The attenuation and magnetic field were recorded in both analog and digital format for analysis and plotting by use of a high-speed digital computer. All experimental curves reproduced in Sec. III are traced from the computer plots.

The magnet used in these experiments had 7-in. poles tapered to 4 in. at the gap. The gap was 1.75 in., which gave a maximum field of about 11 kG. For the very low-field measurements, the steel yoke and poles were replaced by a nonmagnetic frame to eliminate hys-

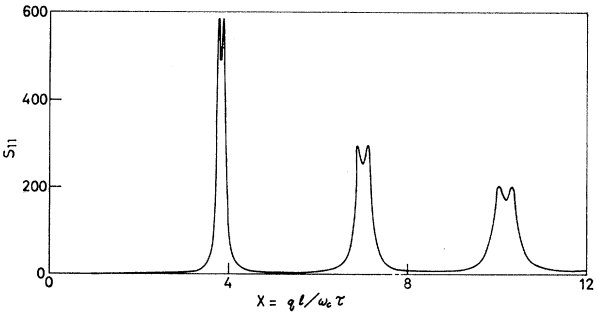

FIG. 2. Calculated attenuation of compressional waves for a cylindrical Fermi surface with **B** parallel to the cylinder axis and perpendicular to **q** for $ql=100$, $\omega\tau=1.0$, or $v_F/v_s=100$.

[6] A. B. Pippard, *The Dynamics of Conduction Electrons* (Gordon and Breach, Science Publishers, Inc., New York, 1965), p. 124.

[7] J. D. Gavenda and B. C. Deaton, Phys. Rev. Letters **8**, 208 (1962).

[8] J. D. Gavenda, in *Progress in Applied Materials Research*, edited by E. G. Stanford, J. H. Fearson, and W. J. McGonnagle (Heywood and Co., Ltd., London, 1964), Vol. 6, p. 43.

teresis. The maximum field attainable was then about 1.5 kG. Magnetic field intensity in either case was measured with a Rawson rotating-coil gauss meter periodically calibrated with NMR equipment.

The single-crystal specimens were grown from a Cd bar purified by zone-refining from stock with a claimed purity of 99.999+%. At the completion of the zone-refining process, silvers were cut from the bar with an acid-string saw to determine the resistivity ratio ($\rho_{300°K}/\rho_{4°2}]_K$). Using a standard four-probe technique, we found it to be in excess of 30 000.

The crystals were oriented to within 0.5° using the Laue back-reflection technique and machined to final size with a spark-erosion machine.

III. EXPERIMENTAL RESULTS

The experimental results are presented in four separate sections. Secs. III A–III C describe and interpret the results related to the portions of the Fermi surface known as the monster, caps, and pillow, respectively; Sec. III D presents evidence for acoustic cyclotron resonance.

A. Monster: Resonant Orbits

1. $\mathbf{q}\|[1\bar{2}10]$

Rather than show the actual curves for attenuation versus magnetic field, we summarize the results for them in terms of caliper dimensions in figures and tables below. However, the attenuation curves for a certain range of the field directions have been found to be quite significant and are presented in Fig. 3. The measurements shown in this figure were made with 70-MHz compressional sound at a temperature of 1.08°K. θ_B refers to the angle between the field direction and the [0001] axis in the plane perpendicular to $\mathbf{q}$. A comparison of the five attenuation curves in this figure

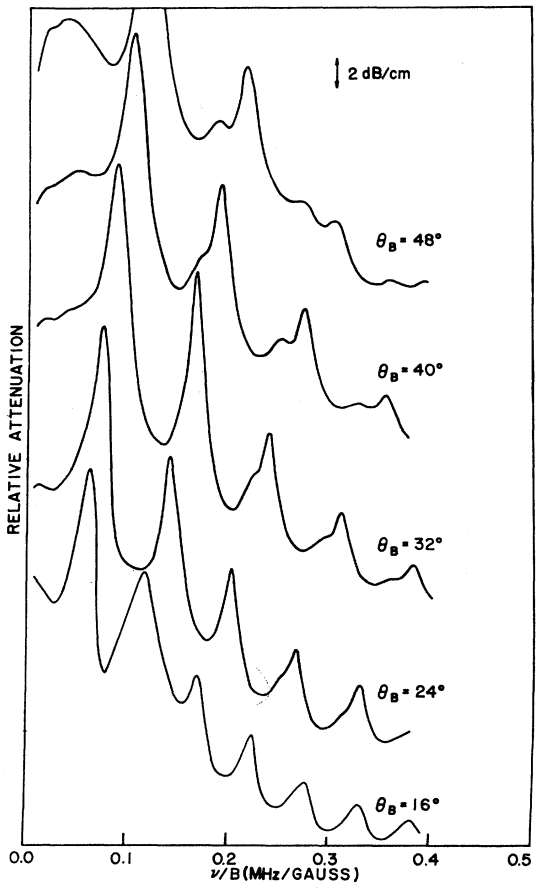

FIG. 3. Attenuation of 70-MHz compressional waves at 1.08°K with $\mathbf{q}\|[1\bar{2}10]$ and $\mathbf{B}\perp\mathbf{q}$. θ_B is the angle between $\mathbf{B}$ and [0001]. In this and the other figures presenting experimental results, the curves have been displaced arbitrary amounts in the vertical direction for clarity.

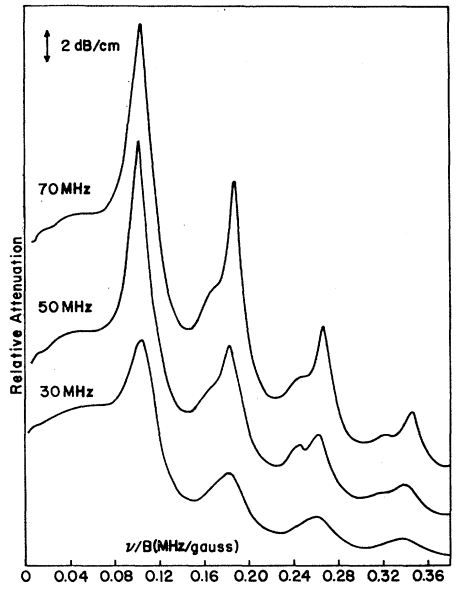

FIG. 4. Frequency dependence of resonances shown in Fig. 3 for $\theta_B=40°$.

shows that the geometric oscillations develop into sharp resonances for θ_B between 24° and 48°.

To see how the resonant peaks change with the frequency of the sound, measurements were made at 1.08°K and $\theta_B=40°$ using frequencies of 70, 50, and 30 MHz. Results of these measurements are presented in Fig. 4. The temperature effects were investigated by comparing the line shapes of the resonances at temperatures of 1.06 and 4.2°K, as shown in Fig. 5 for 110-MHz sound.

These sharp resonances are highly sensitive to the ql value for the experiment, as illustrated by Figs. 4 and 5. At 30 MHz, the oscillations are very much like ordinary geometric oscillations with wide linewidth. At 50 MHz, the broad peaks in the attenuation curve start to break up into two series of oscillations, apparently caused by

two different parts of the Fermi surface with a very small difference in extremal diameter. When the frequency is increased further to 70 MHz, one of the series remains essentially unchanged while the other has attained a large amplitude and a greatly reduced linewidth. The temperature dependence shown in Fig. 5 indicates that the Cd specimen was of such purity that the scattering at 4.2°K was largely due to thermal phonons. When the temperature was lowered to 1.06°K, the mean free path of the electrons increased as a consequence of the reduction in phonon scattering. The resonances become sharper, therefore, as a result of the increased ql value when the sound frequency is increased or the temperature is lowered.

The spacings $\Delta(\nu/B)$ of the successive attenuation maxima for various values of θ_B within this range were

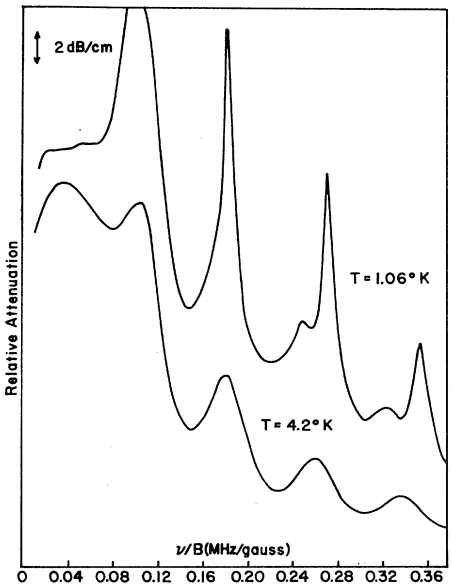

FIG. 5. Temperature dependence of resonances for $\theta_B=40°$, $\nu=110$ MHz.

used to find the momentum values from the relation[8] $k=(ev_s/2\hbar c)[\Delta(\nu/B)]^{-1}$. The k values for the different series within this range are given by the filled circles in Fig. 6.

On the basis of the discussion presented in the Introduction in connection with the possibility of sharp resonances from a cylindrical Fermi surface we conclude that these resonances are associated with a part of the Fermi surface of Cd with a large fraction of orbits having the same extremal diameter perpendicular to the magnetic field direction. Such orbits can be found around the belly of the undulating cylinder on the second-band hole surface as shown in Fig. 7 and marked A. To illustrate the point about nearly equal diameters for different orbits, we choose $\theta_B=45°$ and draw in Fig. 8 the orbit for the plane passing through symmetry point K in the Brillouin zone for the free-electron model.

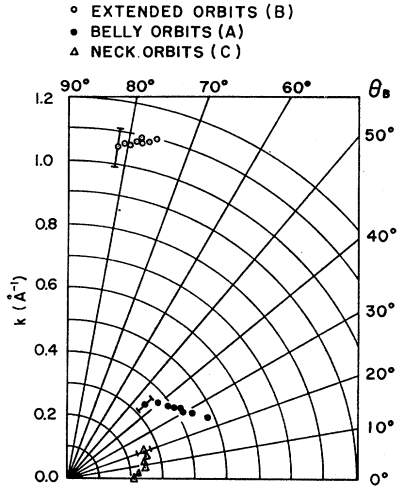

FIG. 6. Half-caliper dimensions of the Cd Fermi surface for various angles θ_B between **B** and [0001]. For the belly and extended orbits (A and B in Fig. 7), **q** is along $[1\bar{2}10]$, and **B** is varied through the $(1\bar{2}10)$ plane. For the neck orbits (C in Fig. 7), shear waves polarized along $[1\bar{2}10]$ were propagated along $[10\bar{1}0]$ and **B** varied within the $(10\bar{1}0)$ plane.

Maintaining the same θ_B, we draw four more orbits on equally spaced planes parallel to the previous one but intercepting line HH in the Brillouin zone at intervals of 0.09 Å^{-1}. The shapes of these orbits are quite similar. Since we are primarily interested in the caliper diameter B_1C_1, only these dimensions are shown in Fig. 8. It can be seen that the deviations among the dimensions B_1C_1 to B_5C_5 are almost negligible. The same situation occurs for other field directions within the 20° range in which the sharp resonances were observed. When θ_B is below this range, orbits around the belly of the undulating

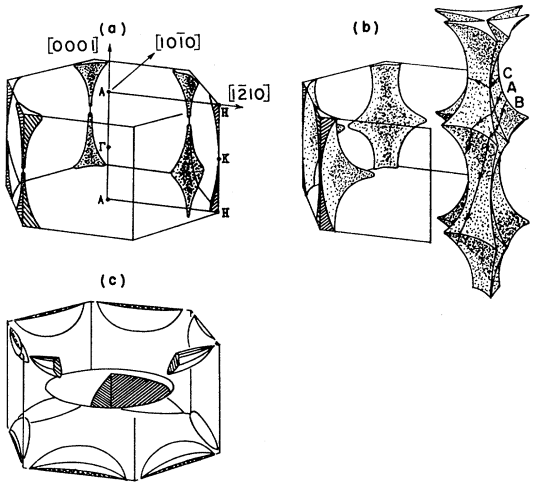

FIG. 7. Cd Fermi surface (based on Fig. 2 in Ref. 11). (a) First-band holes (caps). (b) Second-band holes (monster). (c) Third-band electrons (pillow and butterflies), with fourth-band electrons (cigars) shown cross-hatched. The orbits labeled A, B, and C are referred to in the text as belly, extended, and neck orbits, respectively.

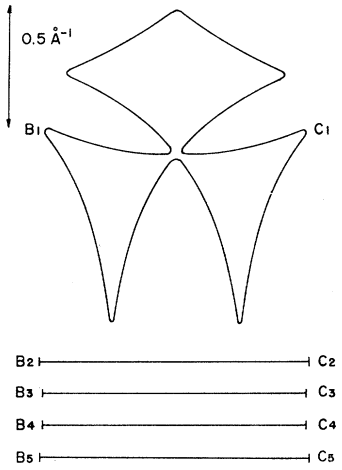

FIG. 8. Orbit for a plane passing through symmetry point K with $\mathbf{B}$ 45° from [0001] in the $(1\bar{2}10)$ plane (A in Fig. 7). With $\mathbf{q}\|[1\bar{2}10]$ the dimension B_1C_1 is calipered. Dimensions for similar orbits on parallel planes (at 0.09 $Å^{-1}$ intervals) are indicated by B_2C_2, etc.

cylinder become impossible. When θ_B is above this range, the characteristic of nearly constant extremal diameter begins to disappear. Because of the complication of mixing with the series of oscillations from the third-band "pillow," the range of 20° is only an approximate value, with a probable error of ±5°. The measured k values in Fig. 6 are in general about 7% smaller than those calculated from the free-electron model. This is not surprising, since we expect the Fermi surface in a real metal will "shrink" down somewhat as a result of energy-band gaps.

When θ_B is further increased, extended orbits around the belly of the undulating cylinder become possible when the magnetic field direction is approximately 15° from $[10\bar{1}0]$. These orbits run from the belly of the undulating cylinder in one zone, cross over the zone boundary and go around the belly in the adjacent zone, as shown in Fig. 7 with the label B. Evidence of extended orbits was found with $\mathbf{q}$ along $[1\bar{2}10]$ in the form of a series of oscillations at the high-field end of the attenuation curves, some of which are shown in Fig. 9. This series of oscillations starts to appear at $\theta_B=74.4°$ and ends at $\theta_B=81.4°$, giving a range of 7°. The k values calculated from the periods of these oscillations are given by the open circles in Fig. 6. The k values and their angular range agree quite well with the proposed orbits on the nearly-free-electron model of Fermi surface. Oscillations from the extended orbits at 1°K were not quite so distinct as those at 4.2°K, apparently because the over-all attenuation at 1°K was very large and tended to obscure the small oscillations in the high-field region. It is believed that this also accounts for the lack of evidence for these extended orbits for $\mathbf{q}$ along $[10\bar{1}0]$, since the attenuation in that case is generally much higher.

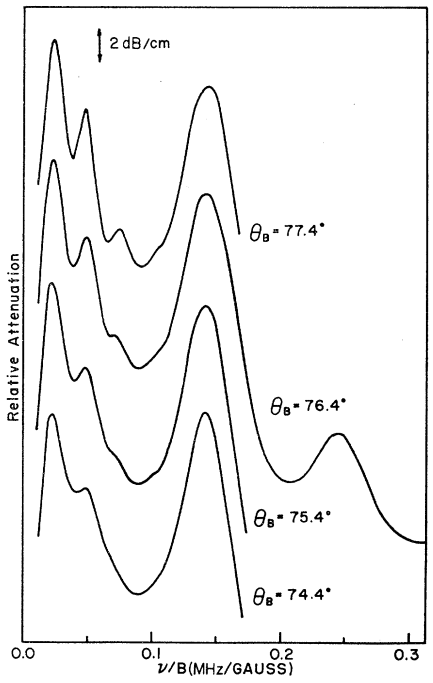

FIG. 9. Magnetoacoustic oscillations at high fields ($\nu/B \lesssim 0.1$ MHz/G) attributed to extended orbits (B in Fig. 7). Measured with 110-MHz compressional waves having $\mathbf{q}\|[1\bar{2}10]$; $\mathbf{B}$ in the $(1\bar{2}10)$ plane, θ_B measured from [0001].

TABLE I. Half-caliper k values of monster waist for $\mathbf{q}$ along $[10\bar{1}0]$.

θ_B(deg)	k values (half-caliper in $Å^{-1}$)
36	0.404
38	0.391
42	0.376
46	0.361
50	0.343

2. $\mathbf{q}\|[10\bar{1}0]$

The over-all attenuation is much larger for compressional waves propagated along $[10\bar{1}0]$. The highest frequency that could be used was 70 MHz. Again only a few selected attenuation curves are presented in this section; the results of the remainder being presented in the form of caliper dimensions in Table I.

Again, resonant peaks in the relative attenuation can be observed for certain values of θ_B although the sharpness has decreased considerably. The variation of these resonant peaks with sound frequency is shown in Fig. 10 at 1.08°K. It should be noted that the scales of the ordinate as well as the abscissa have been reduced by about one-half in this figure as compared to the attenuation curves in Fig. 3 for $\mathbf{q}$ along $[1\bar{2}10]$. In this direction also the resonances disappeared at 4.2°K.

When the sound-propagation direction is $[10\bar{1}0]$, the range of magnetic field orientation is 14° for these resonant belly orbits (from $\theta_B=36°$ to approximately 50°), which is smaller than for $\mathbf{q}\|[1\bar{2}10]$. The k values

calculated from the periods of these resonances, given in Table I, are again about 7% smaller than the free-electron values.

The orbits corresponding to these field directions have shapes similar to that shown in Fig. 8. One of them is illustrated in Fig. 11 for $\theta_B = 39°$, and the caliper dimensions for orbits on three other equally spaced parallel planes are also included. It is seen that the caliper dimensions are indeed nearly equal on different planes perpendicular to the field, although the degree of uniformity is slightly inferior to that for **q** along $[1\bar{2}10]$. The frequency and temperature effects are similar to those for **q** along $[1\bar{2}10]$.

Evidence for orbits around the neck of the monster (marked C in Fig. 7) has been found in shear-wave

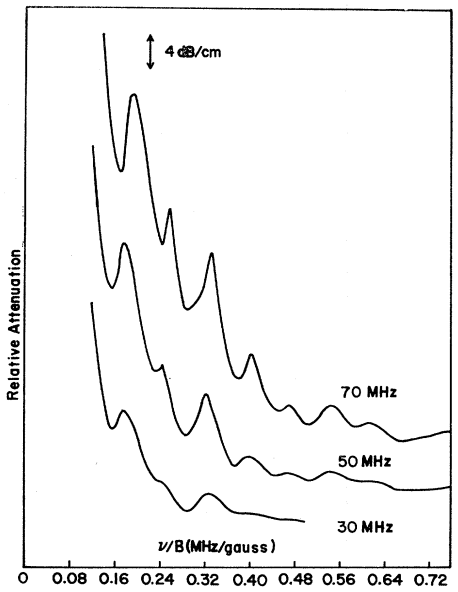

FIG. 10. Attenuation of compressional waves at 1.08°K propagated along $[10\bar{1}0]$ with **B** 36° from [0001] in the $(10\bar{1}0)$ plane, showing resonance amplitudes increasing with frequency.

measurements with **q** along $[10\bar{1}0]$. The values of k calculated from the data are given by Δ in Fig. 6. The measured variation of the k values with θ_B is in good accord with the geometry of the proposed orbits around the neck, three of which are illustrated in Fig. 12.

Probably as a result of the complexity of the orbits associated with the second-band monster, very few magnetoacoustic data on this part of the Fermi surface have been published. Gibbons and Falicov[3] assigned a set of oscillations throughout a range of 30° for θ_B to the "tubes" which were described as the tentacles of the monster. Daniel and Mackinnon[2] showed some of the attenuation curves for their measurements, including some with indications of the sharp resonance peaks, but they did not speculate about their cause. Orbits around the belly of the undulating cylinder were reported by

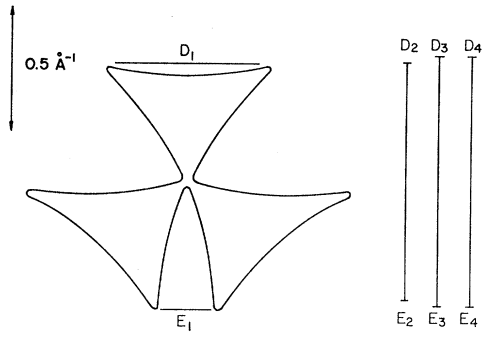

FIG. 11. Orbit for a plane passing through K with **B** 39° from $[000\bar{1}]$ in the $(10\bar{1}0)$ plane. With $\mathbf{q} \| [10\bar{1}0]$ the dimension D_2E_1 is calipered. Dimensions for similar orbits on parallel planes are indicated by D_2E_2, etc.

Anderson and Love[9] as well as by Grassie[10] in de Haas–van Alphen (dHvA) data. Galt *et al.*[4] found the belly orbits and extended orbits by the cyclotron-resonance method. Although the "fluted surface" in their article is not in full agreement with the model we propose, the parts that are relevant to the two types of orbits in question do agree. Tsui and Stark[11] also reported finding the belly and extended orbits by the dHvA method. The magnetic field angular dependence is more fully discussed in their paper. More recently, rf size-effect measurements were made in Cd by Jones *et al.*[12] and by Naberezhnykh *et al.*[13] Evidence for the extended orbits was found, and the dimensions attributed to these orbits agree within 10% with the caliper dimensions presented earlier in this paper.

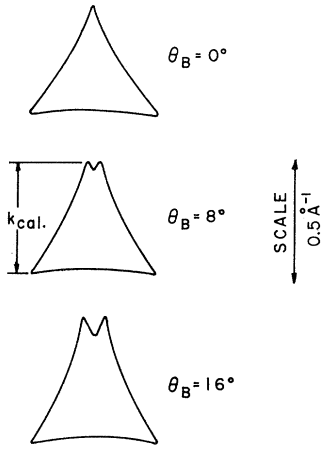

FIG. 12. Neck orbits (C in Fig. 7) for $\mathbf{q} \| [10\bar{1}0]$, **B** in $(10\bar{1}0)$ plane, and θ_B measured from $[000\bar{1}]$.

[9] J. G. Anderson and W. F. Love, Bull. Am. Phys. Soc. **8**, 258 (1963).
[10] A. D. C. Grassie, Phil. Mag. **9**, 847 (1964).
[11] D. C. Tsui and R. W. Stark, Phys. Rev. Letters **16**, 19 (1966).
[12] R. C. Jones, R. G. Goodrich, and L. M. Falicov, Phys. Rev. **174**, 672 (1968).
[13] V. P. Naberezhnykh, A. A. Mar'yakhin, and V. L. Mel'nik, Zh. Eksperim. i Teor. Fiz. **52**, 617 (1967) [English transl.: Soviet Phys.—JETP **25**, 403 (1967)].

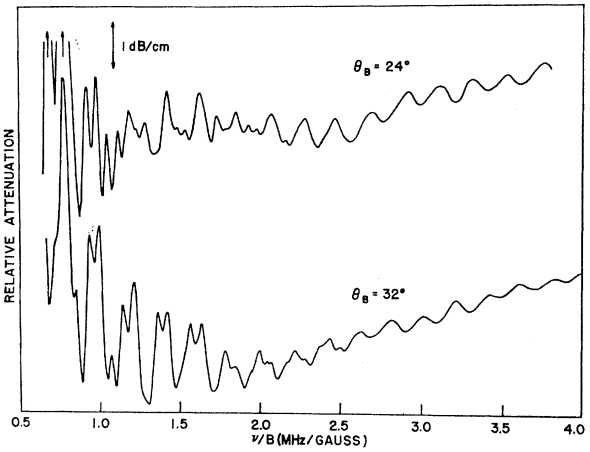

FIG. 13. Attenuation of 70-MHz compressional waves at 1.04°K for $\mathbf{q}\|[10\bar{1}0]$ and θ_B measured from [1000].

B. Caps

No results of magnetoacoustic measurements have been published in connection with the first-band caps (or pyramids) on the Fermi surface of Cd. It is believed that the complexity of the Fermi surface and the consequent intermingling of magnetoacoustic oscillations from different sheets are the main reasons for this. In the present research, the high purity of the specimens was taken advantage of, and measurements were carried out to very low fields. Since $\omega_c\tau$ on different sheets of the Fermi surface may not be the same, the geometric oscillations assigned to the different sheets may start from different magnetic field values in the very low-field region. This characteristic allowed us to sort out oscillations assigned to the third-band pillow and the first-band caps. Oscillations from the latter portion of the Fermi surface start at about 20 G.

1. $\mathbf{q}\|[10\bar{1}0]$

Compressional waves of 70 MHz were used in these experiments which were performed at 1.04°K. The symmetry axes were located by the open-orbit resonance and were accurate to $\pm 0.1°$. Typical results of these measurements showing the presence of two or more periods are presented in Fig. 13.

The values of k calculated from the low-momentum maxima in the measurements are plotted in Fig. 14 in polar form, using a sound velocity of 3.85×10^5 cm/sec. Well-defined oscillations were absent for $\theta_B=0°$. A probable explanation is that, for this magnetic field direction, oscillations from orbits around the neck of the monster are mixed with oscillations caused by the caps which have very similar caliper dimensions.

The k values obtained for $\theta_B=8°$ to 66° are generally 20% smaller than the cavity in the undulating cylinder of the second band in the nearly-free-electron model. This deviation is believed to be largely caused by the energy gap from spin-orbit coupling. The angular variation of these k values is fairly consistent with the shape of the caps although the increase in k value as θ_B is increased is less than expected. This is probably the result of the averaging effects of orbits with different extremal diameters on planes perpendicular to the magnetic field. The same reason may also account for the disappearance of oscillations beyond $\theta_B=66°$, since the caps have quite sharply pointed ends in the [0001] direction.

2. $\mathbf{q}\|[1\bar{2}10]$

With $\mathbf{q}$ along $[1\bar{2}10]$, measurements were made with 70-MHz shear waves polarized along $[10\bar{1}0]$ at 1°K. Some of the results of these measurements are presented in Fig. 15. In these curves two sets of oscillations can be discerned: one set with larger period in the low-field region and one with smaller period in the relatively higher-field region. The latter is mixed with the former set of oscillations at $\nu/B\approx1$ MHz/G.

The results for shear-wave measurements with $\mathbf{q}$ along $[1\bar{2}10]$ illustrate more distinctly the intermingling of oscillations from the third-band pillow and the first-

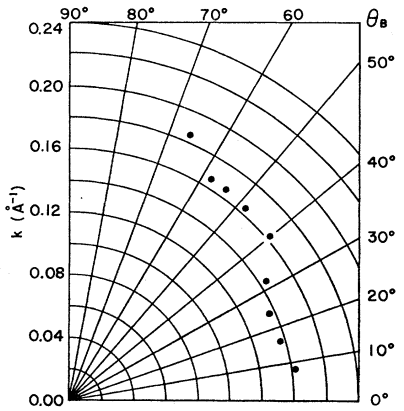

FIG. 14. Fermi-surface half-caliper dimensions for 70-MHz compressional waves with $\mathbf{q}\|[10\bar{1}0]$ and θ_B measured from [0001] in the $(10\bar{1}0)$ plane.

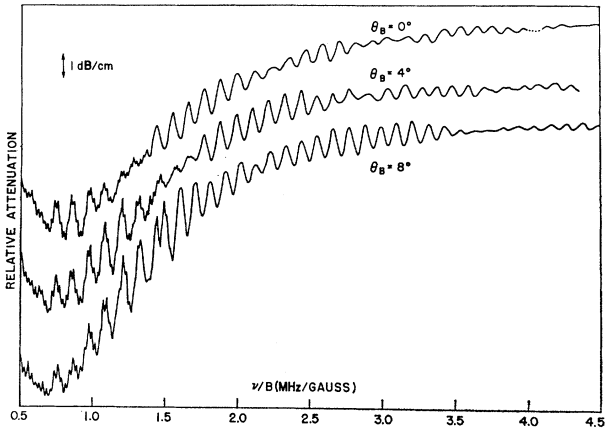

FIG. 15. Attenuation of 70-MHz shear waves at 1.0°K with $\mathbf{q}\|[1\bar{2}10]$, polarization along $[10\bar{1}0]$. θ_B is measured from [0001] in the $(1\bar{2}10)$ plane.

band caps. The k values calculated from the attenuation maxima for the low-field series of oscillations are plotted in Fig. 16 in polar form by use of a sound velocity of 2.23×10^5 cm/sec for this direction. It will be noted that the k values in Fig. 16 for $\mathbf{q}\|[1\bar{2}10]$ are approximately 5% larger than corresponding values in Fig. 14 for $\mathbf{q}\|[10\bar{1}0]$. This is in accordance with the geometry of the caps, since in the case of $\mathbf{q}\|[10\bar{1}0]$ we caliper between one corner of the triangular-shaped cross section and the base, while in the case of $\mathbf{q}\|[1\bar{2}10]$ we caliper between two corners of the triangle. No distinct oscillations appear beyond $\theta_B=42°$ because the shear wave was polarized along $[10\bar{1}0]$ and, as θ_B was increased further, the direction of the magnetic field deviated further from being perpendicular to the polarization vector. Hence, the geometric oscillations gradually died out. The beats that appeared on the attenuation curves in Fig. 15 are either due to mixing with some other orbits or acoustic cyclotron resonance (see Sec. III C).

3. $\mathbf{q}\|[0001]$

The existence of orbits around the first-band caps is further verified by results obtained with $\mathbf{q}\|[0001]$ using both compressional and shear waves. The accuracy of the measurements in this direction is not as good as that obtained in the other symmetry directions since the over-all attenuation is very high and since geometric oscillations are not distinct. The average number of distinguishable maxima is approximately eight for compressional waves. For shear-wave measurements it is less.

There are practically no published magnetoacoustic data for Cd with compressional sound waves propagated along the hexagonal axis. The reason is that the attenuation is extremely large and increases rapidly with field for $\mathbf{B}\perp[0001]$, reaching a level of 40 to 50 dB/cm at 70 MHz even below a magnetic field intensity of 200 G. The rapid increase is believed to be the result of open

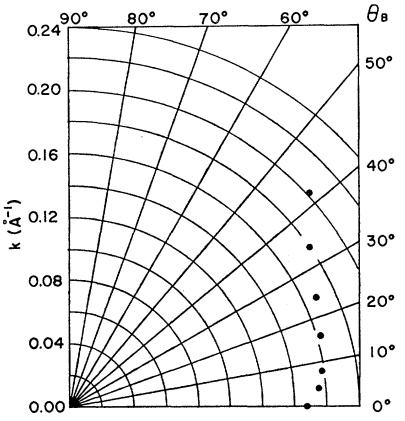

FIG. 16. Fermi-surface half-caliper dimensions for 70-MHz shear waves with $\mathbf{q}\|[1\bar{2}10]$.

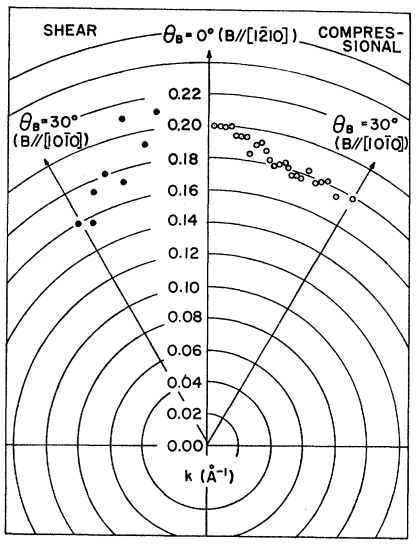

FIG. 17. Fermi-surface half-caliper dimensions for 70-MHz compressional and 50-MHz shear waves with $\mathbf{q}\|[0001]$.

orbits in a constant-phase plane of the sound wave. Deaton[1] interpreted the periods which he observed for this geometry to give the dimensions of the linear extension of the open orbits perpendicular to their direction of motion.

The k values calculated from the attenuation maxima are plotted in Fig. 17 in polar form, using sound velocities of 2.53×10^5 and 1.67×10^5 cm/sec for compressional and shear waves, respectively.

The k values in Fig. 17 are in general agreement with, but approximately 20% larger than, results for the cap orbits with $\mathbf{q}$ along $[10\bar{1}0]$ and $[1\bar{2}10]$. One of the possible reasons for this discrepancy is that the velocity of sound in this direction is actually less than the value assumed. The angular variation of these values precludes other possible orbits. dHvA work by Tsui and Stark[11] also revealed the existence of these cap orbits. Only qualitative agreement can be reached by a comparison of these two concurrent findings, since it is quite difficult to convert the extremal-area data obtained in the dHvA work to the extremal caliper dimensions in our magnetoacoustic measurements for the irregular cross-sectional areas of the first-band caps.

C. Pillow

The series of oscillations in the ultrasonic attenuation pertaining to the third-band pillow of the Fermi surface of Cd have been found to be the most distinct in comparison with series assigned to other parts of the Fermi surface. However, the shape and dimensions of the pillow from the ultrasonic measurements by previous workers are not in agreement. Deaton[1] obtained the cross section of a disc in the $[10\bar{1}0]$ plane as predicted by the free-electron construction, but not in the $[1\bar{2}10]$ plane. Daniel and Mackinnon[2] found that the pillow

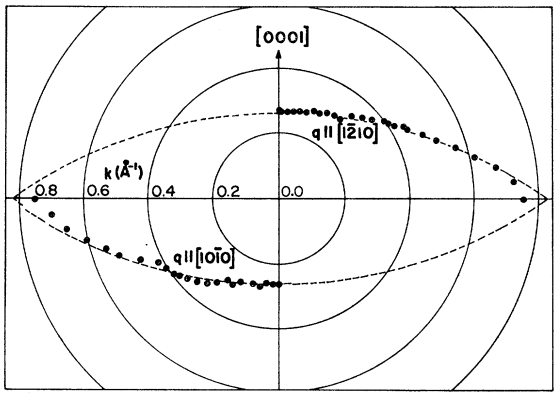

FIG. 18. Fermi-surface half-calipers for $\mathbf{q}\|[1\bar{2}10]$ and $\mathbf{q}\|[10\bar{1}0]$. The dashed line gives the free-electron dimensions.

is disc-shaped, closely resembling the free-electron model, with approximately a 9% reduction in the [0001] dimension and 10% in directions perpendicular to the hexagonal axis. The dimensions of the pillow along the three symmetry axes obtained by Gibbons and Falicov[3] agree quite well with the free-electron model, but they inferred that the pillow had a bump in the center instead of being a smooth disc.

In the present investigation, measurements were made with different frequencies of ultrasound and at various temperatures. Results obtained in the high-field region were compared with those obtained from low-field measurements. The low-field measurements also provided assistance in sorting out oscillations belonging to two or more series arising from different parts of the Fermi surface. For the high-field measurements, the open-orbit resonance was used whenever possible for calibration purposes. The reciprocal-lattice dimension in the direction of the open-orbit resonance is well established, and the magnetic field intensity at which open-orbit resonance occurs can be accurately determined from the well-defined peak in the attenuation curve. Substituting the reciprocal-lattice dimension for

TABLE II. Comparison of k values for pillow obtained by different workers.

Source	k values (half-caliper in Å^{-1}) q along [1$\bar{2}$10] $\theta_B=0°$	q along [1$\bar{2}$10] $\theta_B=90°$	q along [10$\bar{1}$0] $\theta_B=0°$	q along [10$\bar{1}$0] $\theta_B=90°$
Ref. 1	...	0.275	0.778	0.275
Ref. 2	0.729	0.27	0.714	0.249
Ref. 3	0.780	0.275	...	0.270
Present work	0.755	0.271	0.758	0.270
Ref. 12 (RF size effect)	0.781	0.299	0.758	0.276
Ref. 13 (RF size effect)	0.73	0.26	0.73	0.27
Free-electron values	0.829	0.270	0.829	0.270

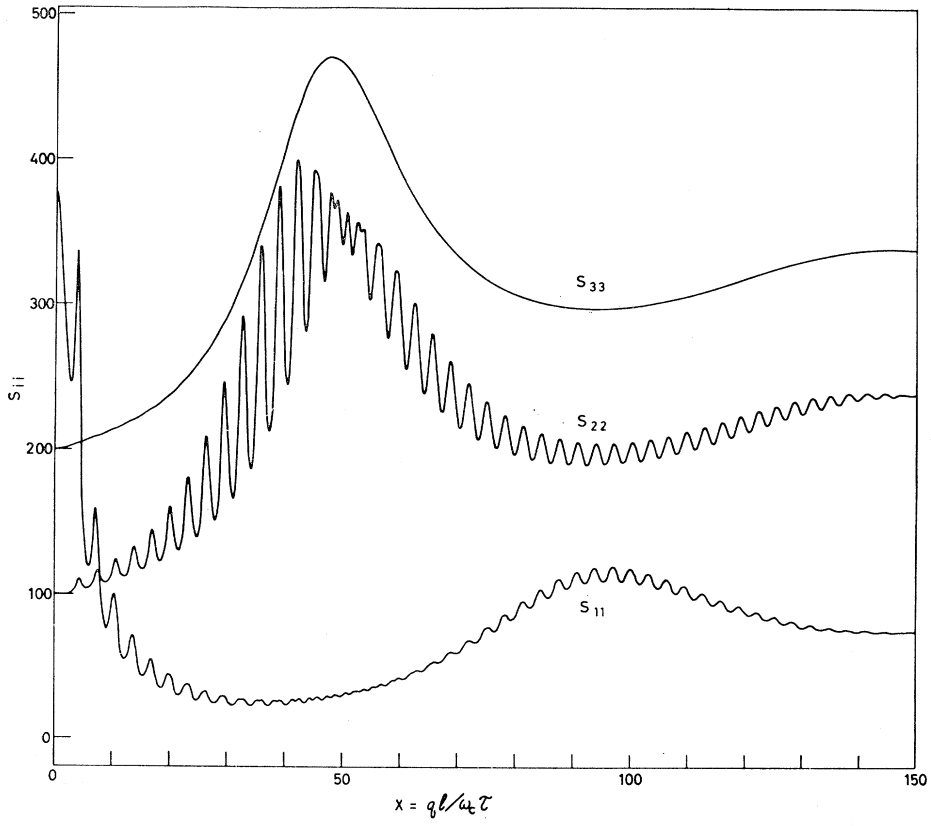

FIG. 19. Attenuation calculated from the results of Ref. 5 for $q\ell=300$, $\omega\tau=3$, or $v_F/v_s=100$. For compressional waves $S_{11}=3S_{ii}/2+30$. For shear waves with $\mathbf{B}$ perpendicular to the polarization $\boldsymbol{\varepsilon}$, $S_{22}=S_{ii}-100$. For shear waves with $\mathbf{B}\|\boldsymbol{\varepsilon}$, $S_{33}=S_{ii}-200$.

p in the equation $p=ev_sB/cv$, the sound wavelength v_s/ν can be determined from the magnetic field intensity B with an accuracy of better than $\pm 0.5\%$.

The momentum values for the pillow are shown in Fig. 18 for propagation along $[1\bar{2}10]$ and $[10\bar{1}0]$. In general, values obtained from the former direction are the more accurate because there are more well-defined oscillations. The accuracies for these values are estimated to be better than $\pm 1\%$ for $[1\bar{2}10]$ and $\pm 2\%$ for $[10\bar{1}0]$ except in directions where there is strong mixing of orbits.

It can be seen in Fig. 18 that the measured values for $\mathbf{q}\|[1\bar{2}10]$ are in close agreement with the free-electron model except for a small range of about 5° from $\theta_B=0°$ where the sharp corner is rounded. Evidence of a bump in the center of the pillow is obviously lacking in this figure. For $\mathbf{q}\|[10\bar{1}0]$, a slight deviation from the free-electron model can be detected at approximately $\theta_B=30°$, but in this region strong mixing of periods occurs, so that the periods are more uncertain. For a comprehensive comparison of results from the different sources, the k values for $\theta_B=0°$ and 90° are listed in Table II for both propagation directions as obtained by different workers including rf size-effect data as well. The spread of k values is seen to be of the order of 5%.

D. Acoustic Cyclotron Resonance

Because of the extremely long electron-relaxation time in our Cd specimens, the condition for acoustic cyclotron resonance[14] (ACR), $\omega\tau \gtrsim 1$, is satisfied at the frequencies employed in these experiments. Features such as the minima near $\nu/B=0.7$ Hz/G were frequently observed. As we reported earlier,[15] even for $\omega\tau=0.5$ ACR has considerable influence on the shape of the attenuation curves. One observes what appears to be "beating" between two nearly equal geometric periods as a result of Doppler shift.

Figure 19 shows the attenuation for the different polarizations calculated from the free-electron model for $\omega\tau=3$. It is helpful to examine the asymptotic expressions for the attenuation in the limit $ql\gg 1$, $X\gg 1$ as derived in Appendix A:

$$S_{11}=\tfrac{1}{6}\pi ql\frac{\sinh(\pi X/ql)[\cosh(\pi X/ql)+(\pi X)^{-1/2}\cos(\pi\omega/\omega_c)\sin(2X-\frac{1}{4}\pi)]}{\sinh^2(\pi X/ql)+\sin^2(\pi\omega/\omega_c)}, \tag{7}$$

$$S_{22}=\tfrac{4}{3}ql\frac{\sinh(\pi X/ql)[\cosh(\pi X/ql)-2(\pi X)^{-1/2}\cos(\pi\omega/\omega_c)\sin(2X-\frac{1}{4}\pi)]}{\sinh^2(\pi X/ql)+\cos^2(\pi\omega/\omega_c)-4(\pi X)^{-1/2}\cosh(\pi X/ql)\cos(\pi\omega/\omega_c)\sin(2X-\frac{1}{4}\pi)}, \tag{8}$$

$$S_{33}=\tfrac{4}{3}ql\frac{\sinh(\pi X/ql)\cosh(\pi X/ql)}{\sinh^2(\pi X/ql)+\cos^2(\pi\omega/\omega_c)}. \tag{9}$$

The ordinary geometric oscillations are the result of the terms including $\sin(2X-\frac{1}{4}\pi)$, while cyclotron resonance occurs for S_{11} when $\omega=n\omega_c$ but, for S_{22} and S_{33}, when $\omega=(n+\frac{1}{2})\omega_c$. Note that the damping terms are functions of $\pi X/ql=\pi/\omega_c\tau$.

Roberts[16] suggested that one can distinguish between ACR and long-period geometric oscillations by comparing results for compressional and shear waves. Since geometric oscillations occur when orbit diameters are multiples of λ, their periods will be different for shear and compressional waves of the same frequency because v_s, and thus λ, is different. However, the period of ACR is determined by ω and is independent of v_s.

We were unable to use this criterion for distinguishing between the two effects because we could not reliably reproduce the field values at which resonances occurred on different experimental runs. We attribute this to failure to have **B** precisely perpendicular to **q**. This produced a net drift velocity of electrons along **q** to introduce an additional unknown Doppler shift.

There are two factors which lead us to believe that the low-field peaks are caused by ACR. First, their amplitudes are extremely mean-free-path-dependent. In most cases, they disappear completely at 4.2°K, although they are quite prominent near 1.0°K. Second, they have a large amplitude for shear waves even when **B** is parallel to the polarization. The free-electron model indicates, as shown in Fig. 19, that geometric oscillations should vanish for this condition; however, the ACR peaks should persist as **B** is brought parallel to the polarization. This is in qualitative agreement with the experimental results.

There is one final comment to be made relating to ACR. Note that, at least for the free-electron model, the resonance condition for shear waves is $\omega=(n+\frac{1}{2})\omega_c$, while for compressional waves it is $\omega=n\omega_c$. Thus, one would not expect to find the first peak at the same value of B for each of the two cases. In our experiments however, we found indications that the first peaks did tend to occur at the same value of B. Until the measurements are repeated with much more precise control of field orientation, however, we cannot yet say whether this represents a failure of the free-electron model, or whether it is just an experimental error.

[14] N. Mikoshiba, J. Phys. Soc. Japan **13**, 759 (1958).
[15] J. D. Gavenda and F. H. S. Chang, Phys. Rev. Letters **16**, 228 (1966).
[16] B. W. Roberts, Phys. Rev. Letters **6**, 445 (1961).

IV. SUMMARY

We have used the magnetoacoustic effect in very pure Cd specimens to determine some of the dimensions of the Fermi surface not hitherto reported or concerning which conflicting data have been published.

We have observed resonances in the attenuation for particular orientations of the magnetic field which we ascribe to portions of the Fermi surface with essentially constant extremal diameter along a finite section of k_z. The resonances are similar in form to open-orbit resonances which likewise result from finite regions of the Fermi surface with constant dimension in $\mathbf{k}$ space.

Finally, because of the high purity of our Cd specimens, we have observed ACR's superimposed on the magnetoacoustic oscillations. We discuss some of the problems which arise in attempts at determining the ACR periods.

ACKNOWLEDGMENTS

We wish to express our appreciation to Dr. J. R. Boyd, Dr. D. B. Doan, and Dr. B. G. W. Yee who, along with W. R. Cox, provided considerable assistance in making the measurements and in carrying out some of the computer calculations.

APPENDIX A

We quote here the principal results from Sec. IV and the appendices of Ref. 5 and then show the principal components of σ_{ij} in the limit $X\gg1$,

$$\sigma_{11}=(3\sigma_0/q^2l^2)[1-(1-i\omega\tau)G(X)], \tag{A1}$$

where

$$G(X)\equiv\sum_{n=-\infty}^{\infty}\frac{g_n(X)}{1+i(n\omega_c-\omega)\tau}, \tag{A2}$$

$$\sigma_{22}=3\sigma_0\sum_{n=-\infty}^{\infty}\frac{s_n(X)}{1+i(n\omega_c-\omega)\tau}, \tag{A3}$$

$$\sigma_{12}=\frac{3\sigma_0(1-i\omega\tau)}{ql}\sum_{n=-\infty}^{\infty}\frac{g_n'(X)}{1+i(n\omega_c-\omega)\tau}, \tag{A4}$$

$$\sigma_{33}=3\sigma_0\sum_{n=-\infty}^{\infty}\frac{r_n(X)}{1+i(n\omega_c-\omega)\tau}, \tag{A5}$$

$$g_n(X)\equiv\int_0^{\pi/2}J_n^2(X\sin\theta)\sin\theta\,d\theta \tag{A6}$$

$$=X^{-1}\left[\tfrac{1}{2}-\int_X^{\infty}J_{2n}(2x)\,dx\right] \tag{A7}$$

$$=\frac{1}{X}\sum_{m=0}^{\infty}J_{2m+2n+1}(2X), \tag{A8}$$

$$g_n'(X)\equiv dg_n(X)/dX, \tag{A9}$$

$$s_n(X)\equiv\int_0^{\pi/2}[J_n'(X\sin\theta)]^2\sin^3\theta\,d\theta \tag{A10}$$

$$=r_n(X)+(4X)^{-1}(d/dX)[Xg_n'(X)], \tag{A11}$$

$$(d/dX)[Xg_n'(X)]$$

$$=J_{2n}'(2X)-X^{-1}J_{2n}(2X)+X^{-1}g_n(X), \tag{A12}$$

$$r_n(X)\equiv\int_0^{\pi/2}J_n^2(X\sin\theta)\cos^2\theta\sin\theta d\theta \tag{A13}$$

$$=\tfrac{1}{2}\{(1-n^2/X^2)g_n(X)+(4X)^{-1}(d/dX)\times[Xg_n'(X)]\}. \tag{A14}$$

We will assume that $ql\gg1$ and examine the expressions for $X\gg1$. Under these conditions we get $\sigma_{12}^2\ll\sigma_{11}\sigma_{22}$, so (2) reduces to

$$S_{11}=\mathrm{Re}(\sigma_0/\sigma_{11})-q^2l^2[3(1+\omega^2\tau^2)]^{-1}. \tag{A15}$$

We use (A1) to obtain

$$S_{11}=\frac{q^2l^2}{3(1+\omega^2\tau^2)}\left[\mathrm{Re}\frac{1+i\omega\tau}{1-(1-i\omega\tau)G(X)}-1\right]. \tag{A16}$$

Since $|(1-i\omega\tau)G(X)|\ll1$ for the conditions given, this expression can be approximated by

$$S_{11}=\tfrac{1}{3}q^2l^2\,\mathrm{Re}G(X). \tag{A17}$$

In order to evaluate $G(X)$ we use the asymptotic expression for the Bessel functions:

$$J_{2n}(2X)=(\pi X)^{-1/2}\cos(2X-\tfrac{1}{4}\pi-n\pi)+O(X^{-3/2}), \tag{A18}$$

and integrate the second term on the right in (A7) by parts. We find

$$g_n(X)=(2X)^{-1}[1+(\pi X)^{-1/2}\times\sin(2X-\tfrac{1}{4}\pi-n\pi)]+O(X^{-5/2}). \tag{A19}$$

One can ignore the higher-order terms in the expansion of $J_{2n}(2X)$, despite the fact that they increase as n/X, because the $g_n(X)$ contribute to the sum appreciably only near $n\omega_c=\omega$, i.e., near $X=n(v_F/v_s)$. Since v_F/v_s is of the order of 100, the higher-order terms can safely be neglected. We now use

$$\sum_{n=-\infty}^{\infty}\frac{1}{1+i(n\omega_c-\omega)\tau}=\frac{\pi}{\omega_c\tau}\coth\left[\frac{(1-i\omega\tau)\pi}{\omega_c\tau}\right] \tag{A20}$$

and

$$\sum_{n=-\infty}^{\infty}\frac{(-1)^n}{1+i(n\omega_c-\omega)\tau}=\frac{\pi}{\omega_c\tau}\mathrm{csch}\left[\frac{(1-i\omega\tau)\pi}{\omega_c\tau}\right] \tag{A21}$$

to evaluate the sum in (A2) and obtain (7).

We find the asymptotic form of $r_n(X)$ through the use of (A12), (A14), (A18), and (A19):

$$r_n(X)=(4X)^{-1}+O(X^{-5/2}). \tag{A22}$$

In this case the oscillatory terms cancel out to a higher order. With (A5) and (A20) we arrive at

$$\sigma_{33}=(3\sigma_0\pi/ql)\coth[(1-i\omega\tau)\pi/\omega_c\tau]. \tag{A23}$$

This can be substituted into (4) to obtain (9).

Finally, we use (A11) and (A22) to get

$$s_n(X)=(4X)^{-1}[1-2(\pi X)^{-1/2}\times\sin(2X-\tfrac{1}{4}\pi-n\pi)]+O(X^{-5/2}). \tag{A24}$$

Using (A3), (A20), and (A21), we obtain

$$\sigma_{22}=\frac{3\sigma_0\pi}{4ql}\left\{\coth\left[\frac{(1-i\omega\tau)\pi}{\omega_c\tau}\right]-2(\pi X)^{-1/2}\operatorname{csch}\left[\frac{(1-i\omega\tau)\pi}{\omega_c\tau}\right]\sin(2X-\tfrac{1}{4}\pi)\right. \tag{A25}$$

Again neglecting σ_{12}^2 in comparison with $\sigma_{11}\sigma_{22}$ we find (3) reduces to

$$S_{22}=\mathrm{Re}(\sigma_0/\sigma_{22}), \tag{A26}$$

from which the result given in (8) follows.

APPENDIX B

Sievert[17] has treated the case of a cylindrical Fermi surface, but since we disagree with some of his asymptotic expressions for the attenuation, we present here some of the major steps in the derivation.

As Sievert showed, the problem becomes two-dimensional for this geometry. The expressions for S_{11} and S_{22} are still given by (2) and (3), and for σ_{11}, σ_{22}, and σ_{12} by (A1)–(A4) (except for the replacement of the factor 3 by 2 wherever it occurs). However, the integrals no longer depend on θ, so we find (A6), (A9), and (A10) reduce to

$$g_n(X)=J_n^2(X), \tag{B1}$$

$$g_n'(X)=2J_n(X)J_n'(X), \tag{B2}$$

and

$$s_n(X)=[J_n'(X)]^2. \tag{B3}$$

We must now evaluate sums of the form

$$S=\sum_{n=-\infty}^{\infty}\frac{f_n(X)}{1+i(n\omega_c-\omega)\tau}. \tag{B4}$$

These can be greatly simplified if we assume $\omega\tau\ll1$, whence

$$S=f_0(X)+2\sum_{n=1}^{\infty}\frac{f_n(X)}{1+n^2\omega_c^2\tau}. \tag{B5}$$

A further simplification can be made if we assume $\omega_c\tau\gg1$

$$S=f_0(X)+\frac{2}{\omega_c^2\tau^2}\sum_{n=1}^{\infty}\frac{f_n(X)}{n^2}. \tag{B6}$$

Using these approximations we find that

$$\sigma_{11}=(2\sigma_0/q^2l^2)\{1-J_0^2(X)-(2/\omega_c^2\tau^2)\textstyle\sum[J_n(X)/n]^2\}, \tag{B7}$$

$$\sigma_{22}=2\sigma_0\{[J_0'(X)]^2+(2/\omega_c^2\tau^2)\textstyle\sum[J_n'(X)/n]^2\}, \tag{B8}$$

and

$$\sigma_{12}=(2\sigma_0/ql)[J_0(X)J_0'(X)+(2/\omega_c^2\tau^2)\textstyle\sum J_n(X)J_n'(X)/n^2]. \tag{B9}$$

These expressions are substituted into (2) [with $\frac{1}{3}q^2l^2$ replaced by $\frac{1}{2}q^2l^2$ and terms in $(\omega_c\tau)^{-4}$ neglected] to obtain (5).

Our Eqs. (5) and (6) differ drastically from Sievert's asymptotic expressions. While he concludes that the heights and widths of the resonances are independent of ql, we find the behavior generally expected for resonances. Furthermore, we obtain identical behavior of S_{11} and S_{22}, while Sievert says they have different functional forms.

[17] P. R. Sievert, Phys. Rev. **161**, 637 (1967).